Effects of dimensionality on the electronic structure of Ruddlesden-Popper chromates $Sr_{n+1}Cr_nO_{3n+1}$

Spencer Doyle,[1] Lerato Takana,[1] Margaret A. Anderson,[1] Dan Ferenc Segedin,[1] Hesham El-Sherif,[2] Charles M. Brooks,[1] Xiaoping Wang,[3] Padraic Shafer,[4] Alpha T. N'Diaye,[4] Ismail El Baggari,[2] William D. Ratcliff,[5,6] Andrés Cano,[7] Quintin N. Meier,[7] and Julia A. Mundy[1,*]

[1]*Department of Physics, Harvard University, Cambridge, Massachusetts 02138, USA*

[2]*The Rowland Institute at Harvard, Harvard University, Cambridge, Massachusetts 02142, USA*

[3]*Neutron Scattering Division, Oak Ridge National Laboratory, 1 Bethel Valley Road, Oak Ridge, Tennessee 37831, USA*

[4]*Advanced Light Source, Lawrence Berkeley National Laboratory, Berkeley, California 94720, USA*

[5]*NIST Center for Neutron Research, National Institute of Standards and Technology, Gaithersburg, Maryland 20899-6100, USA*

[6]*Department of Materials Science and Engineering, University of Maryland, College Park, Maryland 20742, USA*

[7]*Université Grenoble Alpes, CNRS, Grenoble INP, Institut Néel, 25 Rue des Martyrs, 38042 Grenoble, France*

Transition-metal oxides host a wide variety of electronic phenomena that can be significantly influenced by the effective dimensionality of the system under consideration. These include charge, spin, and orbital orderings, as well as unconventional superconductivity. In this context, the Ruddlesden-Popper chromates $Sr_{n+1}Cr_nO_{3n+1}$ emerge as a particularly intriguing series of materials. Formally, the chromium atom displays a rather special 4+ oxidation state throughout the entire series. However, the effective dimensionality changes from quasi-2D to 3D as n increases from 1 to ∞. As a result, the insulating antiferromagnetic behavior observed for $n = 1, 2, 3$ transforms into itinerant antiferromagnetism with reduced transition temperature for the $n = \infty$ end member of the series, i.e., the perovskite $SrCrO_3$. Further, distinct orbital orderings with exotic singlet states have been predicted for these systems. However, the lack of single-crystal bulk or thin-film samples has made experimental progress difficult. Here we demonstrate the synthesis of thin films of the perovskite $SrCrO_3$ and the associated layered chromates via oxide molecular beam epitaxy for $n = 1$ to $n = 5$. Our electrical transport measurements reveal a gradual evolution from a strongly insulating state in Sr_2CrO_4 to a metallic state in the end member $SrCrO_3$. X-ray absorption spectroscopy measurements demonstrate a varying hybridization strength of the Cr^{4+} valence electrons across the series, helping to explain the trend in conduction. Density functional theory calculations further confirm the observed transport trend and identify additional distortions present in the system.

Dimensionality is a powerful tool for manipulating electronic properties in materials. By constraining the thickness of a compound, either through synthesizing ultrathin films or by creating superlattice structures, quasi-two-dimensionality can be imposed on a system. The perovskite oxides in particular are a convenient experimental platform for studies of dimensionality due to the natural superlattice structure, the Ruddlesden-Popper phase. In a Ruddlesden-Popper oxide, typically expressed either as $A_{n+1}B_nO_{3n+1}$ or $(ABX_3)_n(AO)$, n-unit thick slabs of a perovskite structure are repeated, sandwiched between so-called rocksalt layers of AO [see Fig. 1(a) for a schematic]. This structure tends to reduce the electronic dimensionality of the system, as the rocksalt layers act to decouple the perovskite slabs from each other. Ruddlesden-Popper oxides for many choices of A and B site demonstrate a variety of exotic phenomena, from superconductivity to high anion mobility, for application in solid oxide fuel cells to tunable microwave dielectrics [1–3].

Due to the anisotropic layered nature of the Ruddlesden-Popper structures and their thermodynamic proximity to each other, traditional bulk growth techniques are not optimal for realizing phase-pure samples. This is particularly the case for high n: while high-quality bulk samples have been made for relatively low n [4], $n = 4$ is the highest layering Ruddlesden-Popper oxide synthesized in bulk form [5]. In thin films, however, layerings as high as $n = 50$ have been reported [6], enabled by the layer-by-layer growth method of molecular beam epitaxy (MBE).

In this context, $Sr_{n+1}Cr_nO_{3n+1}$ is a particularly appealing platform to explore the role of dimensionality in a correlated oxide. While $SrCrO_3$ is reported to host antiferromagnetic order below 40 K [7], $Sr_3Cr_2O_7$ demonstrates a clear Néel transition at around 210 K [8,9]. So far, Sr_2CrO_4, $Sr_3Cr_2O_7$, and $Sr_4Cr_3O_{10}$ [8–10] have been experimentally realized in powder form, and Sr_2CrO_4 has been synthesized by pulsed laser deposition [11], but no single-crystal bulk or film samples have been reported for any of the strontium chromate Ruddlesden-Popper members greater than $n = 1$. The electronic ground state of $SrCrO_3$ itself was unclear due to conflicting measurements [12]. The synthesis of high-quality thin

*Contact author: mundy@fas.harvard.edu

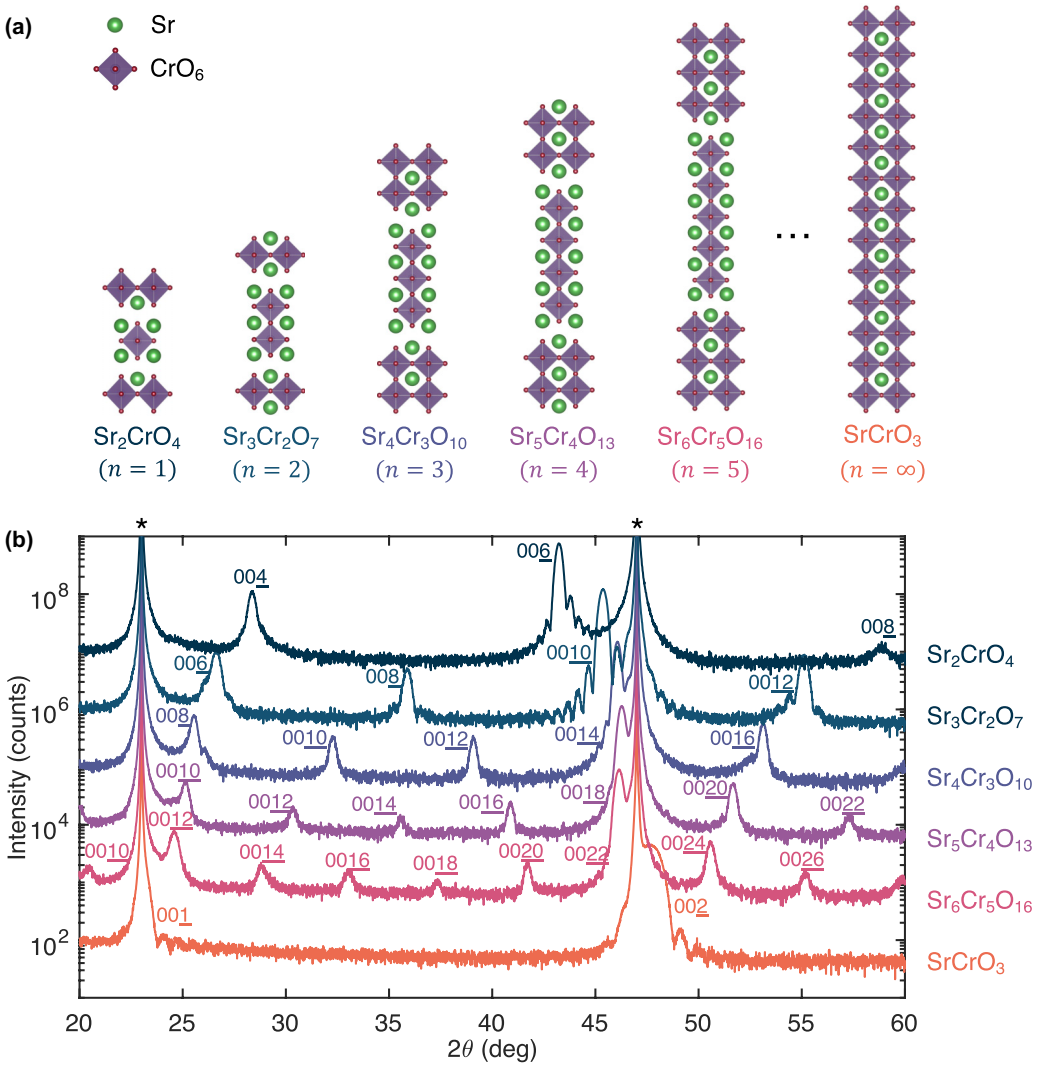

FIG. 1. X-ray diffraction of Sr-Cr-O Ruddlesden-Popper series. (a) Evolution of unit cells across the Ruddlesden-Popper series $Sr_{n+1}Cr_nO_{3n+1}$, from $n = 1$ to $n = 5$, as well as the $n = \infty$ end member, $SrCrO_3$. (b) $\theta - 2\theta$ XRD scans on thin-film samples of the six structures shown in (a). The Miller indices of each peak are labeled for clarity. The $NdGaO_3$ substrate peaks are labeled with asterisks. All films represented here are approximately 20 nm thick.

films of $SrCrO_3$ clarified this dispute, as these samples demonstrated metallic behavior with a low-temperature resistive upturn [13]. The lack of high-quality samples of the Ruddlesden-Popper structures makes verification of theoretical predictions surrounding their ground states complicated. Further, structures with $n > 3$ have not been constructed to date.

In this work we report the synthesis of thin films of the Ruddlesden-Popper series $Sr_{n+1}Cr_nO_{3n+1}$ via oxide MBE. We present x-ray diffraction (XRD) and scanning transmission electron microscopy (STEM) measurements verifying the layered structures. Additionally, we perform electrical transport and x-ray absorption spectroscopy measurements to probe the electronic ground states in this system, demonstrating an evolution from insulating-to-metallic behavior with a rather sudden increase in conductivity from $Sr_4Cr_3O_{10}$ to $Sr_5Cr_4O_{13}$. Finally, we turn to density functional theory (DFT) calculations to study the effects of the increased number of layers (and hence the effective dimensionality) on the electronic, atomic, and magnetic structures.

Synthesis. We synthesized thin films of the $Sr_{n+1}Cr_nO_{3n+1}$ series for $n = 1$–5 and $n = \infty$ on $NdGaO_3$ $(001)_{pc}$ substrates using reactive oxide molecular beam epitaxy (MBE). To the best of our knowledge, $Sr_5Cr_4O_{13}$ and $Sr_6Cr_5O_{16}$ have never been reported in any form before this work. $NdGaO_3$ $(001)_{pc}$ substrates ($a = 3.86$ Å pseudocubic) provide a maximum of 1.0% tensile strain for $SrCrO_3$ ($a = 3.82$ Å) [14] and a minimum of 0.6% tensile strain for Sr_2CrO_4 ($a = 3.84$ Å) [15]. Elemental sources for both strontium and chromium were first calibrated using a quartz crystal microbalance to provide fluxes of approximately 2×10^{13} atoms cm^2/s. We then further refined the dosage by optimizing our $SrCrO_3$ synthesis.

We used a shutter growth scheme in which we alternated depositing strontium and chromium for a deposition time sufficient to deposit one atomic layer. Contrary to previous findings [16], we found that supplying high pressures of oxygen or ozone as an oxidant during growth led to poor film quality, as interpreted from *in situ* reflection high-energy electron diffraction (RHEED) patterns, as well as *ex situ* XRD.

We used an oxygen pressure of 2×10^{-7} Torr and a substrate temperature of about 650 °C as measured with a pyrometer. Our substrates were back-side coated with 200 nm of platinum metal prior to film deposition.

For the layered Ruddlesden-Popper structures, we used the same shutter-type growth but deposited an additional strontium oxide layer every n perovskite unit cells to realize the desired superlattice structures. Other results in the literature on synthesis of strontium-containing Ruddlesden-Popper thin films with oxide MBE have identified a need for an extra layer of strontium oxide at the film-substrate interface [17,18]; we did not find that this was required to realize high-quality films. Whereas the end-member $SrCrO_3$ was stable for strontium:chromium flux ratios up to 10% from unity, the Ruddlesden-Popper structures required the flux ratio to be within about 2% of the ideal stoichiometry. To demonstrate our layering accuracy, we also synthesized an $n = 10$ sample. We provide the corresponding XRD results in the Supplemental Material [19] (see Fig. S2).

We find that we can synthesize high-quality thin films of $SrCrO_3$ on both $NdGaO_3$ $(001)_{pc}$ and $LaAlO_3$ (100) substrates, providing 1% tensile and 1% compressive strain, respectively. We were unable, however, to realize high-quality films of the $n = 1$–5 structures on $LaAlO_3$. In the Ruddlesden-Popper structures, the in-plane lattice parameters expand slightly relative to the perovskite structure. These expanded lattice parameters decrease the tensile strain on $NdGaO_3$ substrates, but increase the compressive strain on $LaAlO_3$. This relatively higher magnitude strain may help explain why $n = 1$–5 phases grow better on $NdGaO_3$ as opposed to $LaAlO_3$. For this reason, all samples represented in this paper are on $NdGaO_3$ $(001)_{pc}$ substrates.

Structural characterization. The structure was characterized by a PANalytical Empyrean x-ray diffractometer at 45 kV and 40 mA with Cu $K\alpha_1$ radiation. Figure 1(b) shows XRD data for $SrCrO_3$ and $Sr_{n+1}Cr_nO_{3n+1}$ from $n = 1$ to $n = 5$. We observe satellite peaks throughout the series, consistent with coherent layer ordering. As n increases, the location of the main diffraction peak shifts to a higher angle, as expected for a decreasing out-of-plane lattice parameter. The thickness fringes seen on the main film peaks indicate a high crystalline quality of the film and a smooth film-substrate interface. We include an atomic force microscopy image of a $Sr_3Cr_2O_7$ film in Fig. S9 to further demonstrate our film quality. The out-of-plane lattice constants as measured by a Nelson-Riley fit are presented in Table I [20]. We include a reciprocal space map of a $Sr_3Cr_2O_7/NdGaO_3$ sample demonstrating epitaxial strain in the Supplemental Material [19] (see Fig. S8).

To characterize the structural quality of our films in real space, we performed high-angle annular-dark-field scanning transmission electron microscopy (HAADF-STEM) and spatially resolved electron energy-loss spectroscopy (EELS) measurements. Electron transparent STEM samples were prepared using a standard focused-ion beam (FIB) lift-out and thinning on a FEI Helios 660. High-angle annular-dark-field STEM measurements were performed on an aberration-corrected Thermo-Fisher Scientific Themis Z G3 operating at 200 kV. The convergence angle for these experiments was 19.6 mrad, and the collection angle range for HAADF conditions was 68–280 mrad. Fast-acquisition frames were collected, aligned, and summed to minimize the effect of sample drift and obtain high signal-to-noise-ratio images. EELS measurements were done on the same instrument, which is also equipped with a Gatan Continuum spectrometer and imaging filter. A dual EELS scheme was used to simultaneously acquire both the Cr-$L_{2,3}$ edge (575 eV) and Sr-$L_{2,3}$ edge (1940 eV), despite the large energy difference between their edge onsets. The chromium and strontium EELS edges were background subtracted up to the relevant elemental edge by modeling the background linear combination of power laws and performing local background averaging to minimize background error [21]. After background subtraction, we integrated the EELS signals for chromium and strontium to obtain 2D chemical maps. The 82×20 pixel EELS map shown in the manuscript was sampled at 0.05 nm/pixel and acquired with a dwell time of 10 ms/pixel to minimize drift while maintaining good signal-to-noise ratio for individual atoms.

TABLE I. Nelson-Riley c lattice parameters extracted from XRD measurements (Fig. 1), calculated c lattice parameters, and band-gap values from Arrhenius plots of resistivity data (Fig. 3) for our Ruddlesden-Popper film series. Our Sr_2CrO_4 films were too insulating for electrical transport measurements; the band-gap estimates in the table are from other works.

Sample	c, meas. (Å)	c, calc. (Å)	Δ, meas. (meV)
Sr_2CrO_4	12.58 ± 0.15	12.60	$100 - 300$ [10, 11]
$Sr_3Cr_2O_7$	20.01 ± 0.06	19.93	74 ± 2
$Sr_4Cr_3O_{10}$	27.8 ± 0.4	27.66	61 ± 2
$Sr_5Cr_4O_{13}$	35.31 ± 0.07	35.06	17 ± 5
$Sr_6Cr_5O_{16}$	43.34 ± 0.11	42.68	5 ± 3
$SrCrO_3$	3.81 ± 0.02	3.78	0

Figure 2 shows a HAADF-STEM image of a $n = 2$ sample, with both the film and the substrate visible in the field of view. The contrast in HAADF-STEM scales with the atomic number, and so the substrate appears brighter as a result of the higher atomic number of the neodymium atoms. The microscopic $n = 2$ layering, whereby the perovskite unit cell is offset by 1/2 unit-cell every two out-of-plane units is visible in both the zoomed-in HAADF-STEM image [Figs. 2(b) and 2(c)] and the EELS chemical maps derived from the Sr-$L_{2,3}$ and Cr-$L_{2,3}$ edges [Fig. 2(c)].

Zooming out, the HAADF-STEM image in Fig. 2(a) shows additional features that cannot be easily deduced from nominally excellent XRD curves or small field-of-view STEM images. In particular, the Ruddlesden-Popper structure exhibits stacking faults in which the rocksalt layer is shifted by half of a unit cell. Such faults occur both laterally and along the imaging direction, in which case the signature appears as a change in HAADF contrast due to imperfect or incoherent stacking of strontium and chromium atoms. Such defects are common in Ruddlesden-Popper structures even under precise shuttering sequences in MBE due to slight imbalances in flux ratios during growth [22].

Electrical transport. Now that we have verified the structural quality of our films, we turn to characterization of their electrical transport properties. Cr(10 nm)/Au(100 nm) electrical contacts were deposited in a Hall bar geometry with

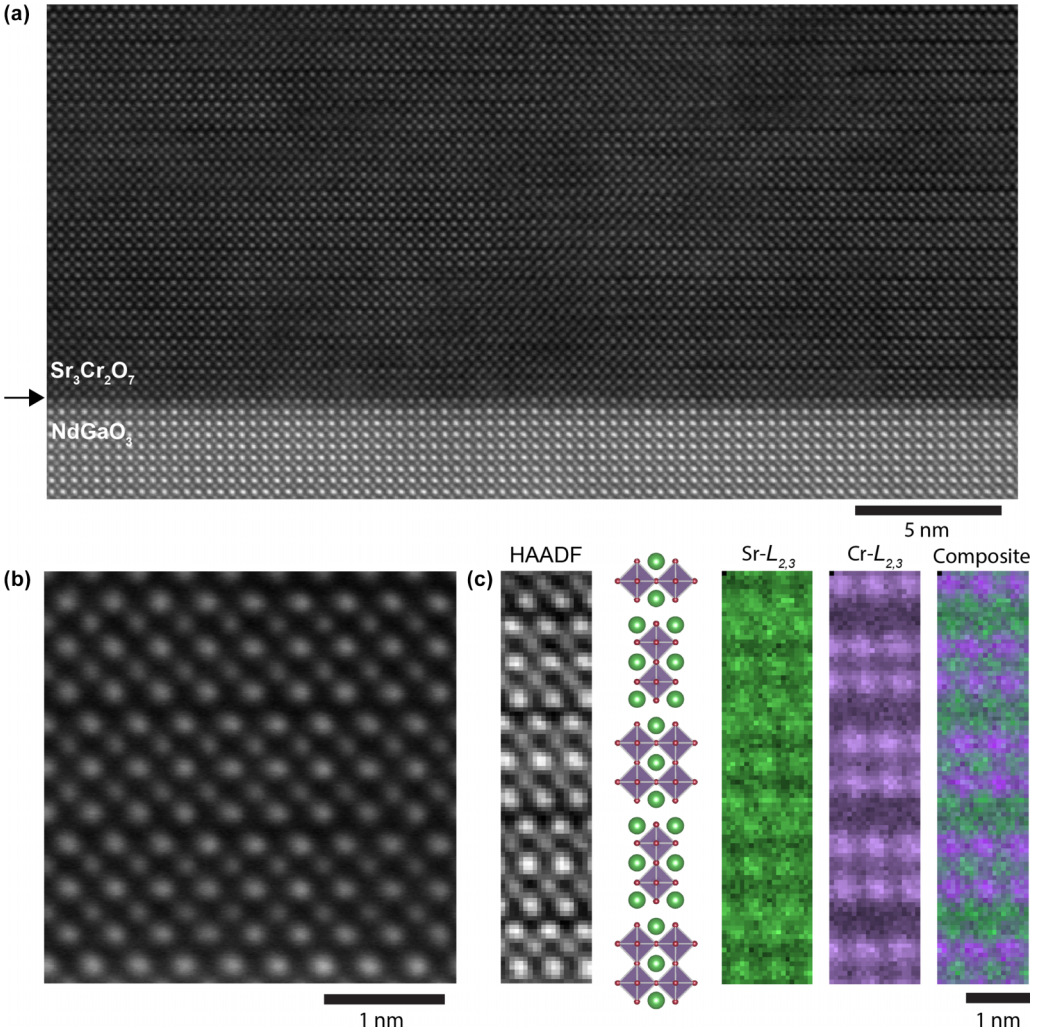

FIG. 2. Elemental and structural characterization of $Sr_3Cr_2O_7$. (a) High-angle annular-dark-field scanning transmission electron microscopy (HAADF-STEM) low-magnification scan of a $Sr_3Cr_2O_7$ film on a $NdGaO_3$ substrate. The arrow demarcates the film-substrate interface. (b) A higher magnification HAADF-STEM scan of the same $Sr_3Cr_2O_7$ film, demonstrating the layered structure. (c) Sr-$L_{2,3}$ edge spectra, Cr-$L_{2,3}$ edge spectra, and composite spectral images from the HAADF image shown. The crystal structure diagram demonstrates the atomic layering visible in the spectra.

an electron-beam evaporator. Channels were etched in with a diamond scribe. A typical device was roughly 3 mm × 5 mm. Transport measurements were performed in a Quantum Design Dynacool physical property measurement system. Hall coefficients were calculated from linear fits of antisymmetrized field sweeps measured from ±9 T. All of our transport results are summarized in Fig. 3. Figure 3(a) demonstrates the resistivity versus temperature behavior of five samples: from $n = 2$ to $n = 5$, and the end member $SrCrO_3$. Our $n = 1$ samples were too insulating as grown to measure with our setup.

$SrCrO_3$ demonstrates metallic behavior with a residual resistivity ratio of approximately 1.6 and a resistive upturn below about 60 K. This behavior is consistent with previous reports on the transport behavior of $SrCrO_3$ thin films [16]. A gradual change in transport behavior is present in the series from Sr_2CrO_4 on the insulating side to $SrCrO_3$ on the metallic side. The resistivity drops abruptly from $Sr_4Cr_3O_{10}$ to $Sr_5Cr_4O_{13}$, with both $Sr_5Cr_4O_{13}$ and $Sr_6Cr_5O_{16}$ demonstrating positive resistivity versus temperature slopes at room temperature, indicative of metallic scattering. Both samples, however, have their resistivities increase at lower temperatures, suggesting that they host semiconductor ground states. As mentioned earlier, $Sr_5Cr_4O_{13}$ and $Sr_6Cr_5O_{16}$ have never been reported in any form before this work to the best of our knowledge. While Sr_2CrO_4, $Sr_3Cr_2O_7$, and $Sr_4Cr_3O_{10}$ have been shown to host antiferromagnetic order [9], the magnetic ground states of $Sr_5Cr_4O_{13}$ and $Sr_6Cr_5O_{16}$ are unknown. Onset of magnetic order may be responsible for the observed change in resistivity versus temperature slope in these compounds, which we predict from DFT calculations later in this work. Experimentally, additional measurements sensitive to antiferromagnetic order would be needed to answer this conclusively.

To further probe the nature of the electronic ground states of the chromate series, we performed magnetic-field-dependent transverse resistivity measurements. The Hall coefficient, R_H, extracted as the slope of the line of best fit

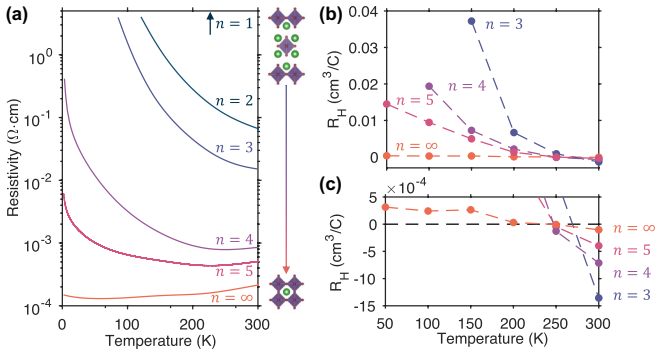

FIG. 3. Demonstration of insulating-to-metallic behavior in $Sr_{n+1}Cr_nO_{3n+1}$ from temperature-dependent electrical resistivity and Hall coefficients. (a) Resistivity vs temperature measured on devices from $n = 2$, $n = 3$, $n = 4$, $n = 5$, and $n = \infty$ samples ($n = 1$ samples were too insulating to measure). The structures on the right demonstrate the progression between the two Ruddlesden-Popper end members: from the insulating $n = 1$, to the metallic $SrCrO_3$. (b) Temperature dependence of the Hall coefficients measured on devices from $n = 3$, $n = 4$, $n = 5$, and $n = \infty$ samples ($n = 1$ and $n = 2$ samples were too insulating for measurement). All four samples demonstrate a change from small-amplitude negative Hall coefficients at high temperatures to larger-amplitude positive Hall coefficients at lower temperatures. (c) A zoomed-in view of the data from (b) to more clearly show the higher-temperature data points. Note the consistent sign change near 250 K throughout the series.

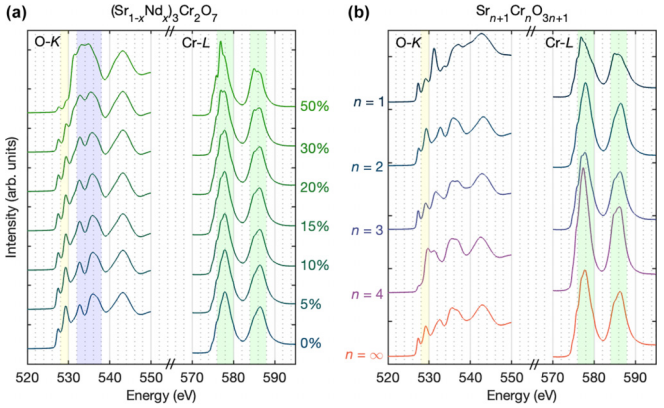

FIG. 4. X-ray absorption spectroscopy. (a) O-K and Cr-L edges for the doping series $(Sr_{1-x}Nd_x)_3Cr_2O_7$. (b) O-K and Cr-L edges for the Ruddlesden-Popper series $Sr_{n+1}Cr_nO_{3n+1}$. The highlighted regions designate the features discussed in the text.

to ρ_{xy} versus B, is plotted in Fig. 3(b). The magnitude of R_H tends to increase for a given sample as the temperature is decreased, indicating fewer charge carriers in the system and matching the semiconducting behavior seen in Fig. 3(a) for those same samples. Compared among samples, the lower n compounds have higher R_H, corresponding to a reduction in charge carriers with reduced dimensionality. This finding is consistent with the behavior seen in resistivity as well.

Additionally, the overall sign of R_H is indicative of the majority charge carrier of a system: positive for majority holelike carriers, negative for majority electronlike carriers. Figure 3(c) provides a zoomed-in view of the R_H values measured at 300 K, demonstrating a consistent change in the sign of R_H at about 250 K for all samples we measured. Strong O $2p$ − Cr $3d$ hybridization is reported to result in delocalized holes in $SrCrO_3$ [23], explaining the predominately holelike conduction in the $n = \infty$ end member. We demonstrate spectroscopic evidence and DFT calculations of such hybridization later in this work.

From the resistivity data in Fig. 3(a), we created Arrhenius plots to extract best-fit band-gap energies Δ. The band-gap values are shown in Table I. The Arrhenius plots are provided in the Supplemental Material (see Fig. S2). The insulating nature of the low-n samples is reported to arise from an orbital ordering that further gaps the chromium t_{2g} states [8,24,25]. We provide our Δ values as an experimental measurement of the strength of this proposed ordering.

X-ray absorption spectroscopy. We performed x-ray absorption spectroscopy (XAS) measurements to study the evolution of the electronic structure in these samples as a function of the layering number. We used Beamline 4.0.2 at the Advanced Light Source at Lawrence Berkeley National Laboratory. Measurements were conducted in the total electron yield geometry with linear x-ray polarization. The polarization was changed from horizontal (I_x) to vertical (I_z), while the angle was fixed at grazing incidence (20°). Each spectra shown represents the average of the horizontal and vertical polarizations, $\frac{1}{2}(I_x + I_z)$, and is the average of 2–6 individual scans. The O-K edge and Cr-L edge spectra were normalized to their respective prepeak intensities. All data presented in Fig. 4(a) was collected during one beamline experiment. All data except for the $n = 2$ measurements in Fig. 4(b) were also collected from one beamline experiment.

Our results are shown in Fig. 4. We nominally expect chromium to be in a 4+ oxidation state across the Ruddlesden-Popper series. Other works have demonstrated that these materials tend to reduce slightly in air, however. While our samples demonstrate consistent transport behavior after weeks in air, implying that no dramatic reduction occurs in our samples, there may be slight reduction at the surface to which transport measurements are insensitive. In an attempt to quantify the scale of reduction, we performed additional XAS measurements on a series that does demonstrate a change in chromium oxidation state: Nd-doped $n = 2$, $(Sr_{1-x}Nd_x)_3Cr_2O_7$. In this compound, Nd^{3+} substitutes for Sr^{2+}, thus resulting in electron doping of the system. These measurements are shown in Fig. 4(a). We note that $Sr_3Cr_2O_7$ has been proposed as a high-T_c superconductor candidate due to the proximity of flat-band regions near the Fermi surface if one could suppress the orbital ordering in the compound [26]. Transport measurements on our Nd-doped series did not demonstrate any signs of superconductivity or increase in conductivity as a result of the electron doping.

In our maximally doped sample (50% neodymium doping), we expect nominally that chromium is in a +3.5 oxidation state, corresponding to the presence of Cr^{3+} and Cr^{4+} sites in roughly equal concentrations. Indeed, the Cr-L_3 and Cr-L_2 edges for our 50% Nd-doped sample both demonstrate splittings with split peak positions of 577 and 578 eV, and 585 and 586 eV, respectively (see green highlighted region).

These energy values match well with the reported energies for Cr^{3+} and Cr^{4+}, respectively [13]. Furthermore, the splitting decreases as the neodymium doping value decreases and disappears entirely in the undoped $n = 2$ sample. Comparing to prior results on $Sr_{1-x}La_xCrO_3$, the Cr-L edges of our $(Sr_{1-x}Nd_x)_3Cr_2O_7$ series demonstrate somewhat more Cr^{3+} character for nominally equivalent neodymium and lanthanum doping values [13]. This can be explained by surface reduction in our samples (XAS measurements were performed several weeks after films were synthesized), or a difference between nominal and actual doping levels in either our samples or the referenced samples. What is clear, however, is an increase in Cr^{3+} character as we increase the amount of neodymium, as expected.

If we use the 50% doped Cr-L edge as a reference spectra and the undoped Cr-L edge as a reference spectra, we can calculate the best-fit linear combination values for the rest of the doping series. These values are plotted in Fig. S3. Additionally, we performed the same linear combination fit for each Ruddlesden-Popper member to estimate the effects of reduction on the series. These results are also plotted in Fig. S3. Here, we complete our discussion of the neodymium doping series before turning to the Ruddlesden-Popper series results.

Turning to the O-K edges, we see two major changes in the neodymium doping series. First, a peak intensity at 529 eV is strongest in the undoped film and weakens consistently as the doping level increases (see yellow highlighted region). This peak has been associated with O 2p-Cr 3d hybridization, which tends to increase with higher oxidation states [27]. Second, we observe two distinct peaks at 533 and 536 eV in the undoped film, which appear to combine into a single split peak in our 50% doped film (see blue highlighted region). These peaks correspond to transitions to the A-site unoccupied d levels [27]. For a pure strontium A site, one should expect transitions to both Sr 4d and Sr 5d levels, resulting in two distinct peaks as we see in our undoped sample. In the case of a neodymium A site, only transitions to the Nd 5d level are expected, as the Nd 4d states are filled. Thus, we interpret the converging peaks centered around 535 eV as representing transitions from O 2p to the changing A-site unoccupied d levels.

With the above results from our $(Sr_{1-x}Nd_x)_3Cr_2O_7$ series, we now turn to the XAS data for our $Sr_{n+1}Cr_nO_{3n+1}$ series shown in Fig. 4(b). Starting with the Cr-$L_{2,3}$ edges, we do not observe a clear trend throughout the series. To compare approximate oxidation states with our neodymium doping series, we performed the same fitting as before using the undoped $n = 2$ sample and 50% doped sample Cr-L edges as reference spectra. Our best-fit linear combination coefficients for the Ruddlesden-Popper series are presented in Fig. S3. These fit values indicate a weak Cr^{3+} character in the series, particularly for the $n = 4$ sample. These slightly reduced oxidation state values might suggest the presence of oxygen deficiencies in our films. Due to the surface sensitivity of the spectroscopy measurements, it is unclear whether such oxygen deficiencies are present only at the surface or throughout the bulk of the films. In the case of $SrCrO_3$, oxygen vacancies rapidly induce insulating behavior [16]. Our grown $SrCrO_3$ films are metallic, as shown in Fig. 3, thus implying that our $SrCrO_3$ samples are fully oxidized in the bulk. Given the consistent evolution in conductivity discussed earlier, it seems likely that our samples all host predominantly Cr^{4+} oxidation states, and thus our slightly reduced oxidation states likely stem from reduced Cr^{3+} ions at and near the film surfaces.

Members of $Sr_{n+1}Cr_nO_{3n+1}$ host antiferromagnetic order with a range of Néel temperatures as high as 210 K in $Sr_3Cr_2O_7$ [8,9]. Sr_2CrO_4 and $Sr_3Cr_2O_7$ are reported to host both spin and orbital orderings [8,24,25,28–30]. With interest in tracking the evolution of these orderings in our series, we performed neutron diffraction measurements at Oak Ridge National Laboratory, attempting to characterize the antiferromagnetic order in a $Sr_3Cr_2O_7$ sample with a thickness of 100 nm. We chose to focus on $Sr_3Cr_2O_7$ given its relatively high Néel temperature. No magnetic order was detectable in our $Sr_3Cr_2O_7$ films with neutron diffraction on the TOPAZ instrument. Given the high structural quality of our samples, we suspect that our lack of observed magnetic ordering is due to the low signal intensity resulting from the low sample volume.

The Ruddlesden-Popper O-K edges demonstrate relative intensity changes in the peak at 529 eV, corresponding to O 2p-Cr 3d hybridization as discussed earlier. It appears that the $n = 2$ and $n = 4$ films have a relatively stronger hybridization, whereas the $n = 1$, $n = 3$, and $n = \infty$ films all have relatively weaker hybridization (see yellow highlighted region). Prior works have suggested an orbital singlet ground state in the $n = 2$ compound that forms vertically between the two adjacent Cr-O layers [8,29]. Such a state is not reported for the $n = 1$ or $n = 3$ compounds, as singlet formation is structurally dependent on the even layering number in the $n = 2$ structure. Additionally, calculations on the $n = 2$ compound suggest it hosts strong O 2p-Cr 3d hybridization with the in-plane oxygen sites [29]. Our results support this claim of strong hybridization and suggest that such hybridization is especially strengthened in even-numbered Ruddlesden-Popper structures. We additionally demonstrate a proposed origin of this layer-dependent hybridization strength in our DFT results, which we turn to now.

Electronic structure calculations. In order to gain additional insight into the electronic and magnetic properties of the $Sr_{n+1}Cr_nO_{3n+1}$ chromates, we turn to DFT. This allows us to better understand the role played by the crystal structure and calculate trends across the series.

Our DFT calculations were performed using VASP [31,32]. We used a converged **k**-point grid of $12 \times 12 \times 12$ for $n = \infty$, scaled down proportionally for $n = 1, .., 5$ compounds with a plane-wave cutoff of 650 eV. For the exchange-correlation part, we use the Perdew-Burke-Ernzerhof (PBE) functional [33]. We use pseudopotentials with the following valence: Sr: $4s^24p^65s^2$, Cr: $3s^24p^63d^54s^1$, O: $2s^22p^4$. In our spin-polarized calculations we use PBE+U in the Liechtenstein approach [34] with a small U (J) of 1 eV (0.1 eV) applied on the Cr 3d orbitals to take into account the additional electronic correlations. The structures were relaxed for a convergence threshold on the forces of 0.01 eV/Å. To connect with the presented experiments, we simulate the epitaxial strain by fixing the in-plane lattice parameter to the experimental value and optimizing the out-of-plane

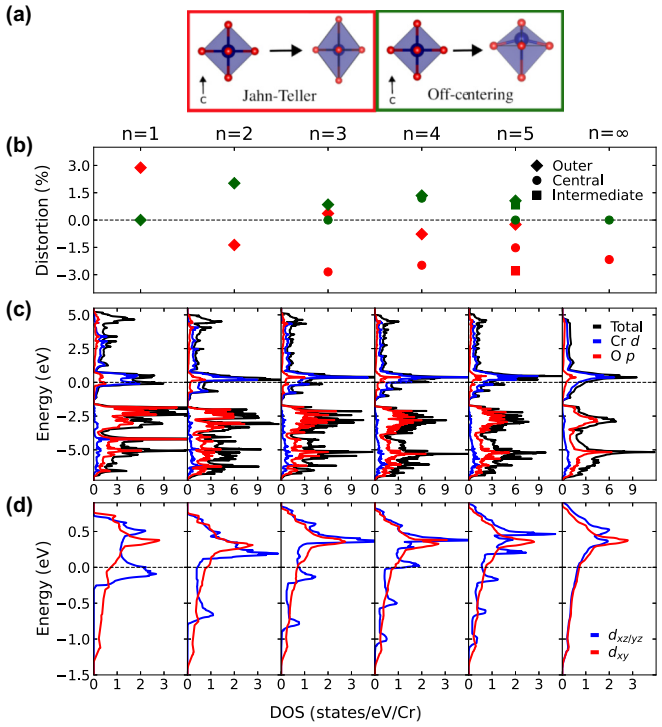

FIG. 5. Relevant distortions of the CrO_6 octahedra and calculated density of states (DOS) across the series (from non-spin-polarized calculations). (a) Sketch of the Jahn-Teller-like and the off-centering distortions of the CrO_6 octahedra. (b) Computed distortions for the different CrO_6 octahedra across the series, where the colors correspond to the boxes in (a). (c), (d) Total and projected DOS.

lattice parameter as well as the internal positions. We quantify the distortions of the Cr-O octahedra in the following sections using the Cr-O bond lengths (see Fig. S5).

Nonmagnetic electronic structure. We start by discussing non-spin-polarized calculations. The crystal structures reported for the Ruddlesden-Popper chromates and their perovskite end member correspond to the $I4/mmm$ and $P4/mmm$ space groups, respectively [35,36]. Accordingly, the CrO_6 octahedra have two main structural degrees of freedom that are relevant to the discussion. These are illustrated in Fig. 5(a). One is a Jahn-Teller-like distortion of the CrO_6 octahedra, while the other is an off-centering of the chromium and equatorial oxygen atoms, both of them perpendicular to the strontium oxide spacer. The former has been reported for $n = 1$ in [8], while the latter is absent for $n = 1$ but has been reported for $n = 2$ in [30]. The presence of these distortions naturally leads to changes in the hybridization between Cr $3d$ and O $2p$ states. In addition, these distortions are expected to lift the degeneracy within the Cr $3d$ states.

We find that the Cr t_{2g} (i.e., Cr $d_{xy/xz/yz}$) derived states are partially filled in all the members of the series, with a non-negligible overlap with the O $2p$ levels near the Fermi level [see Figs. 5(c) and 5(d)]. Thus, the degree of Cr $3d$-O $2p$ hybridization is important for the low-energy physics of these systems. In this respect, we note that the above distortions, and hence their influence on such a hybridization, can be locally different at different chromium layers. The off-centering, in particular, is always zero at the central layer for $n = 1, 3, 5, \ldots$, while it is generally nonzero (but antiparallel) otherwise. Consequently, the relative strength of the Jahn-Teller-like vs off-centering distortions tends to oscillate between odd- and even-numbered compounds. This oscillatory behavior across the series is illustrated in Fig. 5. Although it is difficult to establish a one-to-one correspondence, this behavior is in line with the different Cr $3d$-O $2p$ hybridization in even- vs odd-numbered structures deduced from the XAS measurements.

Next, we take a closer look at the electronic structure of the different compounds in relation to the local environment of the chromium atoms and the above distortions. In particular, we notice that the $d_{xz/yz}$ states are split off from the d_{xy} ones [see Fig. 5(d)]. For large n, the difference is small and essentially comes from the epitaxial strain. As n decreases, however, the bandwidth associated with $d_{xz/yz}$ states becomes much smaller than that associated with the d_{xy} ones (up to $\sim$1 eV vs $\sim$2 eV for $n = 1$). In that case the spacer between the n-layer blocks plays the key role, as it implies reduced overlaps involving the $d_{xz/yz}$ orbitals compared to the d_{xy} ones, such that the former end up being more localized.

To further quantify the difference between these states, we calculate the corresponding crystal-field splitting from the band centroids $E_i = \int \varepsilon N_i(\varepsilon) d\varepsilon / \int N_i(\varepsilon) d\varepsilon$, where N_i is the partial density of states associated with the orbital i. In this respect, the Jahn-Teller-like and the off-centering distortions can be expected to be dominant and subdominant factors respectively, with the spacer playing a role also. The calculated splittings are shown in Fig. S4 for the different chromium layers of these systems. Compared to what would be obtained for an isolated CrO_6 octahedron with the same distortion, a reversed crystal-field splitting implying a distinct $t_{2g}^2 \rightarrow d_{xy}^1 d_{xz/yz}^1$ electronic configuration has previously been reported for $n = 1$ [24,25,30]. Our calculations confirm this result and further show that this special configuration spans the whole series. For $n = 1$, the reversal is obtained because the effect of the Jahn-Teller-like distortion is overcome by the hybridization between the Cr $3d$ and the apical O $2p$ states, resulting in a negative charge-transfer gap for the oxygen atoms shared with the spacer [24]. As n increases, the strength of this crystal-field splitting decreases (for $n = \infty$ the spacer is absent so that the only effect is due to the epitaxial strain-induced distortion).

Spin and orbital ordering. In our non-spin-polarized calculations, all the members of the $Sr_{n+1}Cr_nO_{3n+1}$ series are found to be metallic, in contrast to our experimental results. To address this point, we perform spin-polarized calculations within a DFT+U approximation, where additional correlations within the Cr d orbitals are included via a small Hubbard U of 1 eV. Specifically, we consider A-type, C-type, and G-type antiferromagnetic (AFM) configurations for the $n = 1, 2, 3$ and ∞ compounds.

We first consider these magnetic configurations without any additional distortion of the crystal structure (other than the out-of-plane Jahn-Teller-like and off-centering described before). Thus, we find that among these orders, the ground state corresponds to the A-AFM configuration for $n = 1$, while it is the C-AFM one for $n = 2, 3$ and $n = \infty$. In any case, all these states remain metallic.

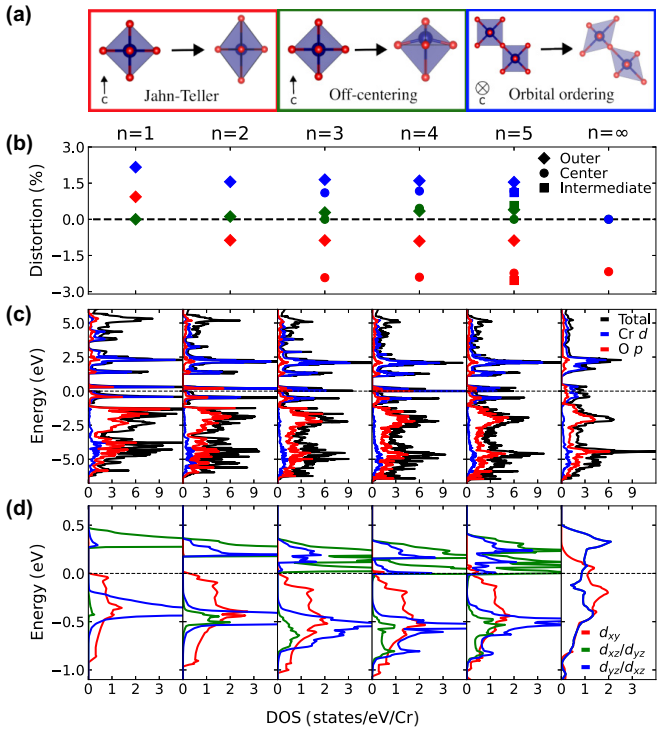

FIG. 6. Relevant distortions of the CrO_6 octahedra for spin-polarized calculations and calculated density of states (DOS) across the series. (a) Sketch of the out-of-plane Jahn-Teller distortion, off-centering of the chromium atoms, and in-plane Jahn-Teller distortion associated with spin-orbital ordering. (b) Amplitude of each of the distortions in the different layers, where the colors correspond to the boxes in (a). (c) The total and site-projected density of states. (d) The orbital projected density of states. The blue and green $d_{xz}d_{yz}$ correspond to the DOS of the d_{xz} or d_{yz} orbitals (alternating in each layer).

Increasing the value of U can lead to insulating behavior as reported in [8,30]. However, we stick to the relatively small $U = 1$ eV and explore additional effects that could lead to insulating behavior in these systems. Carta and Ederer have recently discussed a particular type of spin and orbital ordering for $n = \infty$ under tensile strain [37] which is different from that considered in [8,24,30]. Specifically, the orbital part is associated with the distortion of the CrO_6 octahedra that is illustrated in Fig. 6(a) (see also Fig. S6). This distortion corresponds to an in-plane Jahn-Teller distortion that rotates 90° between neighboring units in the plane. As a result of this distortion, the degeneracy of the $d_{xz/yz}$ orbitals is lifted. Further, the distortions can be aligned or 90°-rotated along the c direction, which determines whether the eventual orbital order is C-type or G-type, respectively.

While it was shown that the distortion vanishes for $n = \infty$ in the absence of strain, we consider the possibility of having this type of distortion in the $n \neq \infty$ members of the Ruddlesden-Popper series. Interestingly, we find that C-type (G-type) AFM order only supports G-type (C-type) orbital order for $n \geqslant 2$ (see Table in Fig. S6). This reveals a direct link between spin and orbital orders in these systems. Furthermore, for $n = 1$ we find that the G-type in-plane Jahn-Teller distortion lowers the energy of the C-AFM configuration below the A-AFM one, which then becomes ground state of the system [see Table in Fig. 6(b)]. This in-plane distortion also emerges in the C-AFM ground state of the other members of the series [see Fig. S6(b)], with an amplitude that decreases as n increases, as shown in Fig. 6(b).

When it comes to the electronic structure, we find that the emergence of such a spin and orbital ordered ground state opens a small gap at the Fermi level leading to semiconducting behavior for $n = 1$ and $n = 2$. This is illustrated in Figs. 6(c) and 6(d) by means of the site-projected density of states. These plots further reveal that there are two key factors leading to the metal-insulator transition across the series: First, there is a further splitting of the d_{xy} orbital and the $d_{xz/yz}$ manifold, such that the d_{xy} states become completely filled; and second, there is an additional splitting of the d_{xz} and d_{yz} manifold due to the in-plane Jahn-Teller distortion (i.e., the orbital ordering). This behavior is in tune with our experimental transport measurements in Fig. 3.

Finally, the analysis of our calculations reveal the following interplay between the other distortions of the CrO_6 octahedra and the electronic properties. First, we find that the out-of-plane Jahn-Teller-like distortion is reduced (especially for $n = 1$) compared to the metallic case, which could explain the temperature dependence of the inverse Jahn-Teller effect reported in [8]. Second, and even more drastically, we find that the off-centering of the chromium atoms next to the spacer, which is very pronounced in the non-spin-polarized state [Fig. 5(b)], is greatly reduced in the spin and orbital ordered ground state [Fig. 6(b)]. This feature is most likely linked to the polar nature of this displacement. Their antiparallel alignment leads to bound charges in the material. If the system is metallic, these charges are eventually screened. However, when the system becomes insulating, these charges tend to remain unscreened. This produces large internal electric fields, making the off-centering distortions unfavorable.

This latter interplay is particularly pronounced for $n = 2$, where the off-centering is large in the absence of spin-and-orbital ordering—when the system remains metallic—but vanishes completely in the presence of such an ordering when the system becomes insulating [see Figs. 5(b) and 6(b)]. For $n \geqslant 3$ some off-centering remains, which has interesting implications on the electronic structure of these systems which are illustrated in Fig. 6. For $n = 3$, in particular, the local DOS of each chromium remains gapped. However, the screening of the internal field leads to a band bending that is large enough to bring the system to a semimetallic state (see Supplemental Material [19], Fig. S7). For $n > 3$, the gap remains open for the chromium next to the spacer, but it closes for the inner ones since there are d_{xy} states at the Fermi level (thereby contributing to the metallicity).

Conclusion. We report synthesis and characterization of a set of thin films across the $Sr_{n+1}Cr_nO_{3n+1}$ Ruddlesden-Popper series. Our results show a continuous increase in conductivity by increasing the number of chromium layers n within the unit cell of these systems, from the low-temperature insulating behavior of the $n = 1$ and $n = 2$ members. This observation is analyzed in relation to the emergence of spin and orbital ordering. Specifically, using density functional theory, we calculate structural and electronic modifications across the series with and without magnetic order. Thus, we identify the emer-

gence of a distinct in-plane Jahn-Teller distortion linked to antiferromagnetic order that further produces an n-dependent gap in the electronic structure at the Fermi level that matches the metal-insulator transition across the series. Further, the calculations reveal a strongly n-dependent off-centering of outer chromium atoms towards the spacers, which depends on the metallic vs insulating character of the system. This off-centering further influences the degree of hybridization between the Cr d and O p states. In fact, our XAS data suggest a strong hybridization between these states that is different in the different members of the series. These combined experimental and theoretical findings expand the field's understanding of a particularly intriguing material system and identify new features of interest deserving of additional work.

The data presented in the figures and other findings of this study are available from the corresponding authors upon reasonable request.

Acknowledgments. We thank Jennifer E. Hoffman for feedback on the manuscript. We thank Scott A. Chambers and Hanjong Paik for experimental advice on synthesis of chromate thin films. This research is primarily supported by the U.S. Department of Energy (DOE), Office of Basic Energy Sciences, Division of Materials Sciences and Engineering, under Award No. DE-SC0021925. This work used resources of the Advanced Light Source, which is a DOE Office of Science User Facility under Contract No. DE-AC02-05CH11231. Device fabrication work was performed at Harvard University's Center for Nanoscale Systems (CNS), a member of the National Nanotechnology Coordinated Infrastructure Network (NNCI), supported by the National Science Foundation under NSF Grant No. 1541959. S.D. acknowledges support from NSF Graduate Research Fellowship Grant No. DGE-1745303 and the STC Center for Integrated Quantum Materials, NSF Grant No. DMR-1231319. D.F.S. acknowledges support from NSF Graduate Research Fellowship No. DGE-1745303. W.R. acknowledges support from the Department of Commerce. J.A.M. acknowledges support from the Packard Foundation and Gordon and Betty Moore Foundation's EPiQS Initiative through Grant No. GBMF6760. Electron microscopy was carried out through the use of the MIT.nano facilities at the Massachusetts Institute of Technology. H.E.-S. and I.E.B. were supported by the Rowland Institute at Harvard. Computational resources were provided by the GRICAD supercomputing center of Université Grenoble Alpes and GENCI Grant No. 2022-AD010913948. A.C. and Q.N.M. acknowledge support from the LANEF Chair of Excellence program.

S.D., L.T., C.M.B., and J.A.M. synthesized the thin films. S.D., L.T., and J.A.M. performed the electrical measurements. M.A.A., H.E.-S., and I.E.B. characterized the samples with scanning transmission electron microscopy and electron energy-loss spectroscopy. S.D., D.F.S., A.T.N., and P.S. performed x-ray spectroscopy measurements. L.T., W.D.R., and X.W. performed neutron diffraction measurements. Q.N.M. and A.C. performed density functional theory calculations. S.D. and J.A.M. conceived and guided the study. S.D., A.C., Q.N.M., and J.A.M. wrote the manuscript, with discussion and contributions from all the authors.

The authors declare no competing interests.

[1] G. Amow and S. J. Skinner, J. Solid State Electrochem. **10**, 538 (2006).

[2] C.-H. Lee, N. D. Orloff, T. Birol, Y. Zhu, V. Goian, E. Rocas, R. Haislmaier, E. Vlahos, J. A. Mundy, L. F. Kourkoutis, Y. Nie, M. D. Biegalski, J. Zhang, M. Bernhagen, N. A. Benedek, Y. Kim, J. D. Brock, R. Uecker, X. X. Xi, V. Gopalan *et al.*, Nature (London) **502**, 532 (2013).

[3] G. A. Pan, D. F. Segedin, H. LaBollita, Q. Song, E. M. Nica, B. H. Goodge, A. T. Pierce, S. Doyle, S. Novakov, D. C. Carrizales, A. T. N'Diaye, P. Shafer, H. Paik, J. T. Heron, J. A. Mason, A. Yacoby, L. F. Kourkoutis, O. Erten, C. M. Brooks, A. S. Botana *et al.*, Nat. Mater. **21**, 160 (2022).

[4] J. Zhang, A. S. Botana, J. W. Freeland, D. Phelan, H. Zheng, V. Pardo, M. R. Norman, and J. F. Mitchell, Nat. Phys. **13**, 864 (2017).

[5] S. Liu, M. Avdeev, Y. Liu, M. R. Johnson, and C. D. Ling, Inorg. Chem. **55**, 1403 (2016).

[6] M. R. Barone, M. Jeong, N. Parker, J. Sun, D. A. Tenne, K. Lee, and D. G. Schlom, APL Mater. **10**, 091106 (2022).

[7] L. O. San-Martin, A. J. Williams, J. Rodgers, J. P. Attfield, G. Heymann, and H. Huppertz, Phys. Rev. Lett. **99**, 255701 (2007).

[8] J. Jeanneau, P. Toulemonde, G. Remenyi, A. Sulpice, C. Colin, V. Nassif, E. Suard, E. Salas Colera, G. R. Castro, F. Gay, C. Urdaniz, R. Weht, C. Fevrier, A. Ralko, C. Lacroix, A. A. Aligia, and M. Núñez-Regueiro, Phys. Rev. Lett. **118**, 207207 (2017).

[9] H. Nozaki, H. Sakurai, I. Umegaki, E. J. Ansaldo, G. D. Morris, B. Hitti, D. J. Arseneau, D. Andreica, A. Amato, M. Månsson, and J. Sugiyama, in *Proceedings of the 14th International Conference on Muon Spin Rotation, Relaxation and Resonance (μ + SR2017)* (Journal of the Physical Society of Japan, 2018).

[10] H. Sakurai, J. Phys. Soc. Jpn. **83**, 123701 (2014).

[11] J. Matsuno, Y. Okimoto, M. Kawasaki, and Y. Tokura, Phys. Rev. Lett. **95**, 176404 (2005).

[12] J.-S. Zhou, C.-Q. Jin, Y.-W. Long, L.-X. Yang, and J. B. Goodenough, Phys. Rev. Lett. **96**, 046408 (2006).

[13] K. H. L. Zhang, Y. Du, P. V. Sushko, M. E. Bowden, V. Shutthanandan, S. Sallis, L. F. J. Piper, and S. A. Chambers, Phys. Rev. B **91**, 155129 (2015).

[14] E. Castillo-Martínez, A. Durán, and M. Alario-Franco, J. Solid State Chem. **181**, 895 (2008).

[15] T. Baikie, Z. Ahmad, M. Srinivasan, A. Maignan, S. S. Pramana, and T. White, J. Solid State Chem. **180**, 1538 (2007).

[16] K. H. L. Zhang, Y. Du, P. V. Sushko, M. E. Bowden, V. Shutthanandan, L. Qiao, G. X. Cao, Z. Gai, S. Sallis, L. F. J. Piper, and S. A. Chambers, J. Phys.: Condens. Matter **27**, 245605 (2015).

[17] J. H. Lee, G. Luo, I. C. Tung, S. H. Chang, Z. Luo, M. Malshe, M. Gadre, A. Bhattacharya, S. M. Nakhmanson, J. A. Eastman, H. Hong, J. Jellinek, D. Morgan, D. D. Fong, and J. W. Freeland, Nat. Mater. **13**, 879 (2014).

[18] Y. F. Nie, Y. Zhu, C.-H. Lee, L. F. Kourkoutis, J. A. Mundy, J. Junquera, P. Ghosez, D. J. Baek, S. Sung, X. X. Xi, K. M. Shen, D. A. Muller, and D. G. Schlom, Nat. Commun. **5**, 4530 (2014).
[19] See Supplemental Material at http://link.aps.org/supplemental/10.1103/PhysRevMaterials.8.L071602 for additional experimental and computational details.
[20] J. B. Nelson and D. P. Riley, Proc. Phys. Soc. **57**, 160 (1945).
[21] P. Cueva, R. Hovden, J. A. Mundy, H. L. Xin, and D. A. Muller, Microsc. Microanal. **18**, 667 (2012).
[22] E. E. Fleck, M. R. Barone, H. P. Nair, N. J. Schreiber, N. M. Dawley, D. G. Schlom, B. H. Goodge, and L. F. Kourkoutis, Nano Lett. **22**, 10095 (2022).
[23] K. H. L. Zhang, P. V. Sushko, R. Colby, Y. Du, M. E. Bowden, and S. A. Chambers, Nat. Commun. **5**, 4669 (2014).
[24] T. Ishikawa, T. Toriyama, T. Konishi, H. Sakurai, and Y. Ohta, J. Phys. Soc. Jpn. **86**, 033701 (2017).
[25] B. Pandey, Y. Zhang, N. Kaushal, R. Soni, L.-F. Lin, W.-J. Hu, G. Alvarez, and E. Dagotto, Phys. Rev. B **103**, 045115 (2021).
[26] D. Ogura, H. Aoki, and K. Kuroki, Phys. Rev. B **96**, 184513 (2017).
[27] J. Suntivich, W. T. Hong, Y.-L. Lee, J. M. Rondinelli, W. Yang, J. B. Goodenough, B. Dabrowski, J. W. Freeland, and Y. Shao-Horn, J. Phys. Chem. C **118**, 1856 (2014).
[28] M. Rani, H. Sakurai, S. Okubo, K. Takamoto, R. Nakata, T. Sakurai, H. Ohta, A. Matsuo, Y. Kohama, K. Kindo, and J. Ahmad, J. Phys.: Condens. Matter **25**, 226001 (2013).
[29] A. A. Aligia and C. Helman, Phys. Rev. B **99**, 195150 (2019).
[30] J. Jeanneau, P. Toulemonde, G. Remenyi, A. Sulpice, C. V. Colin, V. Nassif, E. Suard, F. Gay, R. Weht, and M. Núñez-Regueiro, Europhys. Lett. **127**, 27002 (2019).
[31] G. Kresse and J. Furthmüller, Phys. Rev. B **54**, 11169 (1996).
[32] G. Kresse and D. Joubert, Phys. Rev. B **59**, 1758 (1999).
[33] J. P. Perdew, K. Burke, and M. Ernzerhof, Phys. Rev. Lett. **77**, 3865 (1996).
[34] A. I. Liechtenstein, V. I. Anisimov, and J. Zaanen, Phys. Rev. B **52**, R5467 (1995).
[35] E. Castillo-Martínez and M. Ángel Alario-Franco, Solid State Sci. **9**, 564 (2007).
[36] A. C. Komarek, T. Möller, M. Isobe, Y. Drees, H. Ulbrich, M. Azuma, M. T. Fernández-Díaz, A. Senyshyn, M. Hoelzel, G. André, Y. Ueda, M. Grüninger, and M. Braden, Phys. Rev. B **84**, 125114 (2011).
[37] A. Carta and C. Ederer, Phys. Rev. Mater. **6**, 075004 (2022).